HIGH SPEED TEST RIG FOR IDENTIFICATION OF GAS JOURNAL BEARING PERFORMANCE: DESIGN, CONSTRAINTS, AND FABRICATIONS

by

Sergio Diaz
Dr. Luis San Andrés

May 1999

TRC-RD-1-99

EXECUTIVE SUMMARY

Further advancements in high performance turbomachinery operating at extreme temperatures, hot or cold, mandate the development of gas (foil and herringbone) bearings to procure compact units with improved efficiency in an oil-free environment. Some of the current applications encompass air propulsion jet engines and auxiliary power units (*APUs*), space propulsion and life support systems, micro gas turbines, ceramic *ICE*s and flywheel energy storage units. Likewise, high-speed air conditioning compressors and miniature data storage systems become feasible only if inexpensive gas herringbone bearings replace ball bearings having inherent life limits. Current demands from environmental protection laws require the development of spiral grooved face seals for petrochemical compressor applications effectively minimizing harmful leakage and entirely eliminating oil-lubricated sealing.

Historically, experimental data and experience from gas bearings and seals at low speeds have compared well with theoretical predictions. However, test results from high-speed, turbulent flow foil bearings consistently defies predictions from restrictive computational models. The major reason for discrepancies lies in the questionable extension of limited analytical models to complex configurations where structural effects, fluid compressibility and volume compliance, flow turbulence, and gas rarefaction effects at the molecular scale dominate. The need for improved analysis becomes urgent as demonstrated by the practice of manufacturers to test every mechanical component, openly acknowledging the limited worth of current numerical models.

Along with the need for better analytical models is the need for reliable and significant experimental measurements of the dynamic performance of high speed rotors supported on gas bearings. During the first year of this project, a new test facility has been designed. The test rig consists on a rigid rotor supported on gas bearings and driven by an electrical motor at variable speeds up to 100,000 rpm. High-frequency, high-sensitivity displacement sensors measure the shaft motion at two axial planes in the horizontal and vertical directions. An infrared tachometer registers the shaft speed on the whole range of operation. Three load cells sense the forces transmitted through one of the gas bearings. The general arrangement allows for easy interchangeability of the bearing elements so that different designs can be tested. Special attention has been put into ensuring overall safety of the test rig operation at high speeds.

During the second year of this project, the test rig construction will be completed. Run-up and coast-down tests with increasing levels of disk imbalances will be performed to measure the rotordynamic forced response and to extract equivalent stiffness and damping coefficients of the air bearings. Experiments are also aimed at determining the lift-off speed and "break" torque at which the rotor runs freely on a hydrodynamic air cushion created by the air bearings.

TABLE OF CONTENTS

LIST OF FIGURES

1. INTRODUCTION

Increasing requirements of efficiency, power, and space urge the development of small size, high-speed, lightweight turbomachinery. Modern auxiliary power units (*APUs*), airplane's air conditioning units, turbochargers, turbocompressors, and cryogenic or high temperature applications are some of the critical applications where designers are already seeking alternative forms of lubrication or supports for the rotating parts. In these applications, the use of traditional oil lubricated bearings and seals is impractical, or even impossible in some cases, due to the extreme temperatures, reduced clearances, high velocities, environmental concerns, and the added weight and volume intrinsic to the lubrication system. The use of process gas bearings emerges as a practical option to solve all this problems. Bearings and seals that employ the process gas as lubricant eliminate added weight of oil pumps and reservoirs, reduce the risk of contamination, and can operate at extreme temperature conditions.

Since the 1970's, the airplane industry has been employing gas foil bearings in high speed *APUs* and air conditioning units demonstrating the applicability of this technology as a reliable and cost-effective option. However, very little is known about the operation of foil and gas bearings in general, as evidenced by the manufacturer's requirement to test every design before it is actually implemented. Under the operating conditions of these bearings, thermal effects, turbulence, mechanical deformation, dry and hysteretic friction, and gas rarefaction due to the smallness of the film thickness are important parameters that affect the performance of the bearing. To date, there is not a mathematical model or predictive tool accounting for this parameters, which prevents or at least retards the implementation of process gas bearings in more industrial applications that are awaiting for a reliable alternative solution to traditional oil lubrication.

The main concern about gas bearings is their rotordynamic performance. The gas film itself does not provide significant damping and, due to the smallness of the film thickness, the bearing stiffness is mainly given by the compliance of the housing. Therefore, in compliant bearings the main source of energy dissipation or damping is related to dry friction and/or hysteresis on the flexible parts. The limited literature available on the topic shows that the

predominant vibration of rotors supported by gas bearings is subsynchronous, meaning that the system is out of the linear stable range. However, limit cycles are reached that allow "stable" operation of the machine at very high speeds for long periods of time, which would not be possible with oil lubricated ball bearings. The comprehension of this operating regime is precisely the weakest point in the understanding of the operation of gas foil bearings, as it occurs in the operation of floating ring bearings. Yet, many other parameters like lift-off speed, surface coatings, and rarefaction of the gas at the atomic level due to the small clearances and high speeds also need to be addressed before a conclusive description of gas bearings can be produced.

There is a need for experimental evaluation of the effects of these parameters on the performance of gas bearings to support further development of numerical models and to provide design guidelines. Tests targeting individually the effects of different mechanisms of friction (dry or hysteretic), surface coatings, and flexibility of the foil, for example, will improve our current understanding of these devices and provide solid ground for the development of sound theoretical models. However, to perform tests that replicate actual operating conditions represents a technical challenge by itself. A careful selection of the instrumentation is imperative to ensure that the high frequency, extreme temperature, and small displacement and gap ranges are covered.

2. OBJECTIVES

- To provide the TAMU Rotordynamics Laboratory with a test facility where different configurations of high speed gas bearing and/or gas seal configurations could be tested. The test rig consists of a rigid rotor supported on air bearings and driven by an electrical motor installed at the midspan. A top test speed of 100,000 rpm can be obtained, with a maximum power of 1 KW, to study the rotordynamic behavior of the rotor supported on the test bearings. Two disks allow for introduction of controlled unbalance to excite the two rigid rotor modes. Microdisplacement eddy current sensors detect the rotor motion at several locations and an infrared pick-up measures the shaft speed.

- To perform run-up and coast-down tests with increasing levels of disk imbalances for different gas bearing configurations to study the effects of surface coating, bearing flexibility, clearances, and energy dissipation mechanisms. Equivalent stiffness and damping coefficients will be extracted from the rotordynamic force response when possible. The onset of subsynchronous vibration will be recorded, if any. Analysis of the time records of the displacements and orbits will help understand the forces acting on the rotor while operating with subsynchronous vibrations. Amplitude and frequency characteristics of the limit cycles will be reported. The lift-off speed will also be recorded for each case.

- To develop a computational model for gas bearings that considers fluid compressibility, turbulence, thermal effects, mechanical and thermal deformations, dry and/or hysteretic friction, and dynamic coupling between journal motion, lubricant flow and mechanical deformations. Transient solutions of the rotor-bearings motion will be compared to the experimental measurements to evaluate the prediction of subsynchronous vibration and limit cycles.

Upon completion of the project, better understanding of the gas foil bearing technology will be achieved. Comparisons of theoretical predictions and experimental measurements will be available. The non-linear operating regime with subsynchronous vibrations will be described and characterized. General guides for selection of instrumentation suitable for these applications will be discussed. Moreover, a test rig for high speed testing of gas bearings and seals will be available for further research at Texas A&M University.

3. TEST RIG DESIGN

3.1 Description

A test rig for the study of the rotordynamic performance of gas bearings has been designed. The rig is intended to represent the operation of a rigid rotor supported on gas bearings at high speeds allowing for the measurement of rotor vibrations, operating speed, forces transmitted through the bearings and overall air supply and discharge pressures. Figure 1 shows a cutaway view of the test rig design depicting the overall configuration. A sturdy rotor runs on two air bearings driven by an electrical motor mounted directly on the shaft at the midspan. The rotor, depicted in Figure 2, consists of a solid shaft, 15 mm diameter and 190 mm long, on which the electric motor and two solid sleeves (19 mm diameter) are mounted by press-fitting. The shaft and sleeves are manufactured in normalized 4140 steel. The base structural material of the motor rotor is aluminum.

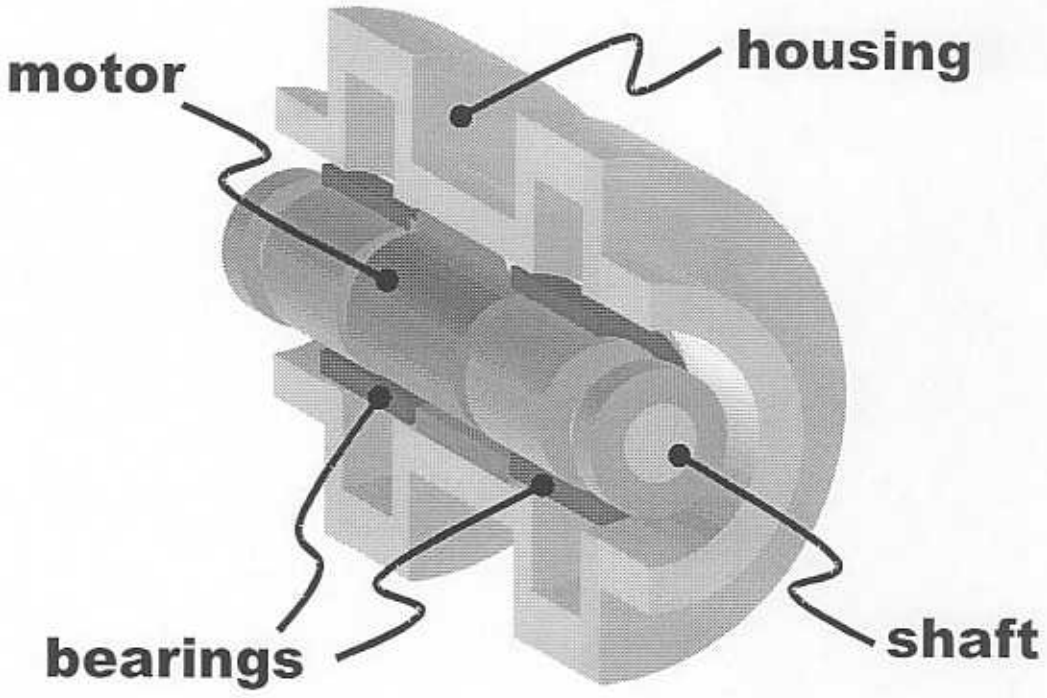

Fig. 1. Cutaway view of the test rig

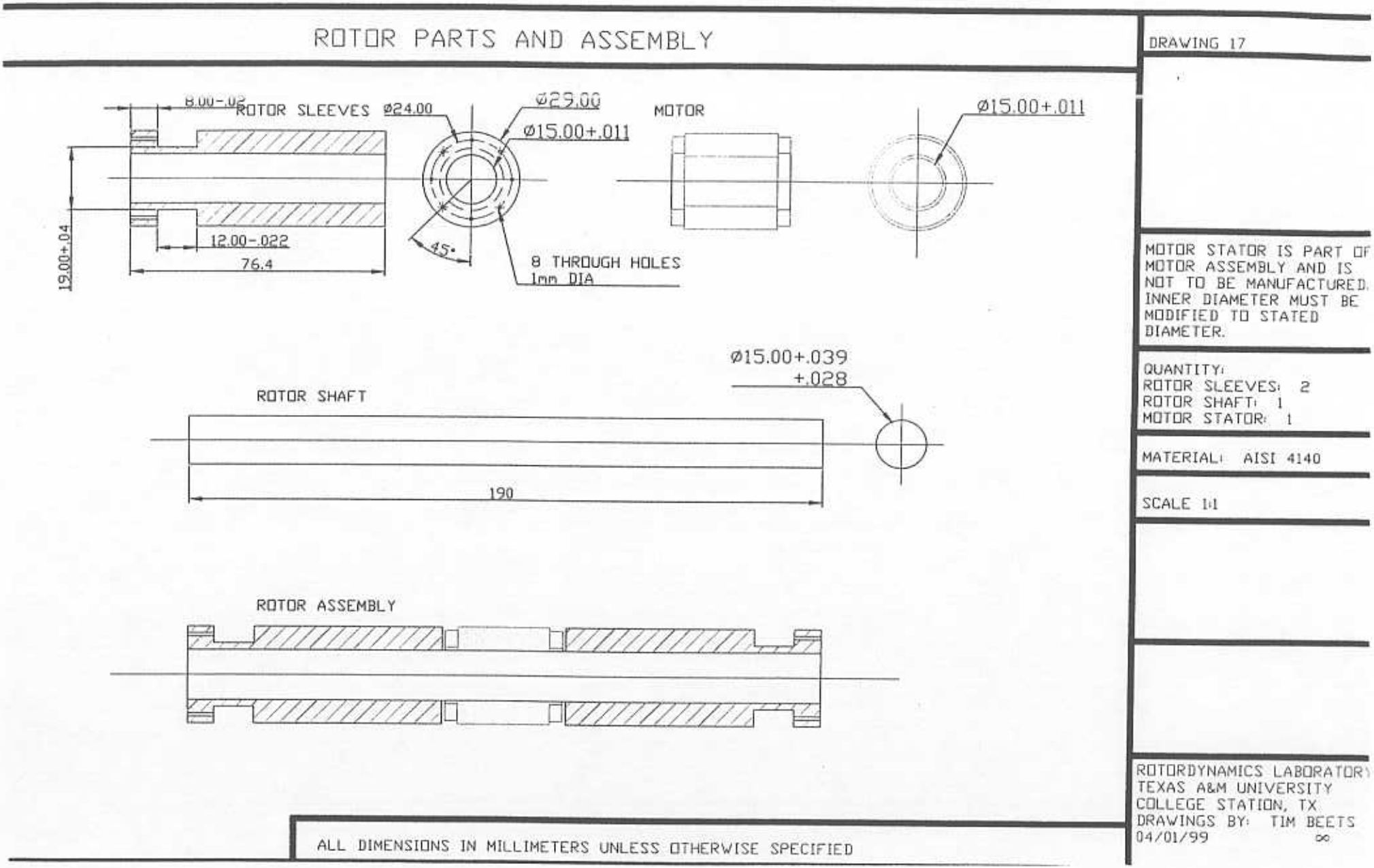

Fig. 2 Test rig rotor

Eight holes at each end of the rotor allow for the placement of imbalance weights. Due to the extremely high operation speed, the imbalance holes are designed of small diameter (1 mm) and the imbalance weights are made out of nylon, whose density is much lower than that of steel allowing for better control of the imbalance magnitude. The electric motor is a commercial two-pole high-frequency motor element with a top speed of 100,000 rpm and maximum continuous power of 1.7 KW. The high frequency converter motor drive allows accurate control of the motor speed by regulating the frequency of the electrical current supplied to the motor. The motor can operate at temperatures up to 150 °C. Yet, excessive heating of the motor can affect its efficiency, thus reducing it output power. Given the small loads that the motor will drive in the test rig, it is not anticipated that forced cooling will be needed. However, the design contemplates the possibility of wrapping the test rig central section with flexible piping to provide water cooling in case of necessity.

Figure 3 shows the overall assembly of the test rig. Two gas bearings, L=30mm, D=29mm, support the rotor, with the electric motor at the midspan. The rotor is dimensioned so that it can be introduced or removed axially with minor disassembling of the rig. It is only required to remove on of the end covers in order to gain access to the shaft. This configuration allows the alignment of the bearings and electric motor without the rotor in place, greatly simplifying this procedure. Each bearings element is installed on a split bearing support (Figure 4) allowing for easy interchangeability of different types of bearings. O'ring type seals installed on the bearing supports divide the rig in several compartments as shown in Figure 3. Each compartment has reversible air ports that can be used as inlet or outlets depending on the configuration being tested. Bourdon type pressure gauges are also installed to register the pressure within the different compartments. The bearing supports also feature a circumferential groove to be used as a feeding channel when hydrostatic bearings are being tested.

Three flat surfaces are machined on the bearing supports circumference, 120° apart from each other, where three swivel-pad support bolts uphold the assembly as depicted in the axial section of Figure 5. One of the bearings is instrumented with high sensitivity piezoelectric load cells to sense the load transmitted to through the bearing. Table 1 contains the main characteristics of the selected sensors. Their high sensitivity, resonant frequency and structural

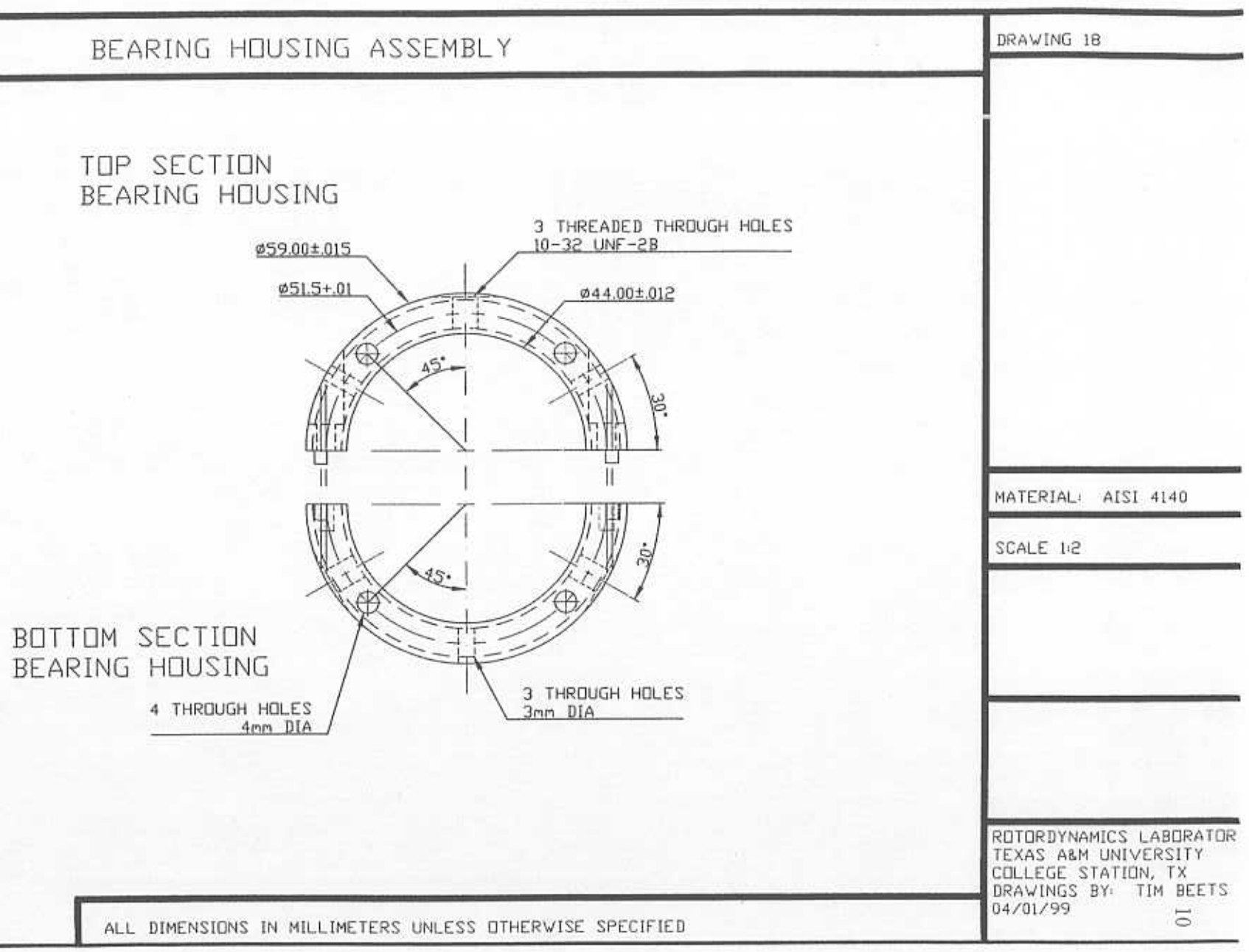

Fig. 4 Split bearing support

stiffness, along with their short rise time and excellent resolution make these load cells ideal for this application where high frequencies, small loads and high precision are demanded.

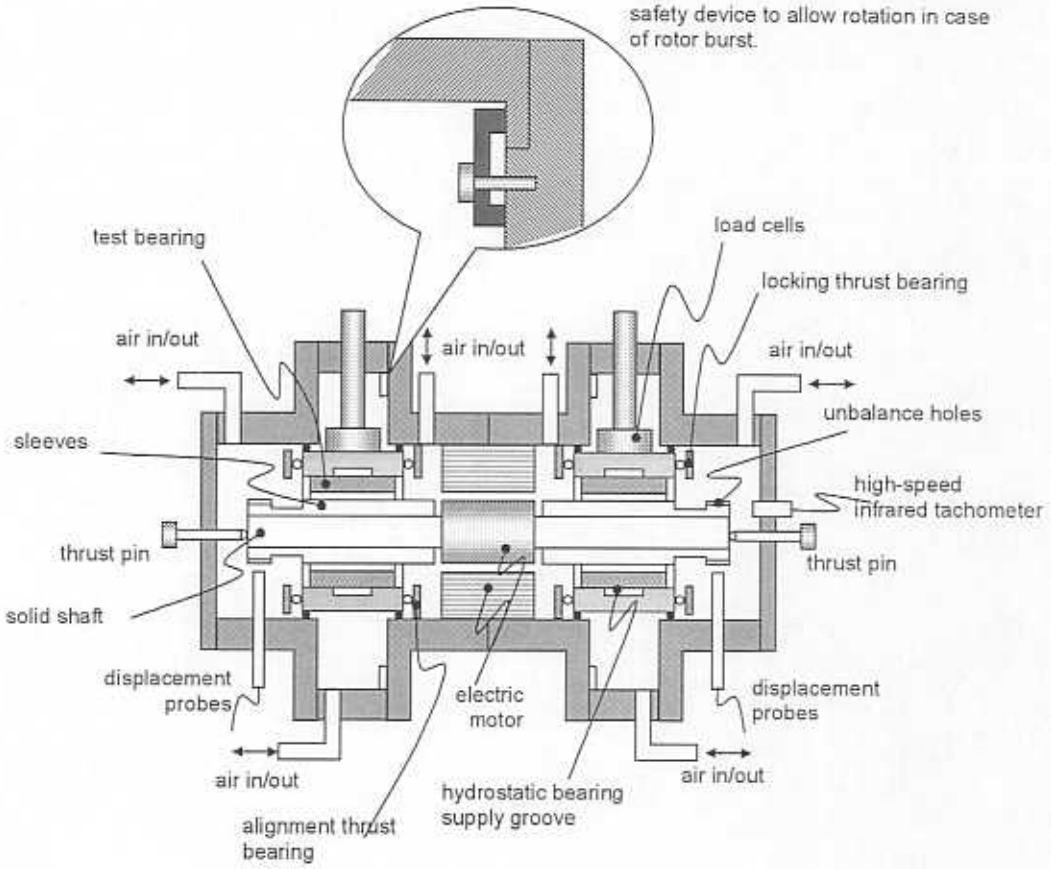

Fig. 3. Test rig assembly

Besides providing support to the bearings and the preload required for the load cells to work properly, the swivel-pad bolts are an integral part of the alignment and centering mechanism. Thrust ball bearings are installed between the bearing supports and flat tracks machined integrally on the rig housing. These ball bearings provide precise axial positioning of the bearings and prevent them from tilting, forcing the two bearings to be perfectly parallel, but do not restrict in any way the radial motion of the bearings. Locking thrust bearings are mounted

on the outboard side of the bearing supports pressing them against the alignment thrust bearings (see Figure 3). The three support bolts adjust the centering of the bearings but do not affect the axial positioning or tilting of the bearing assemblies.

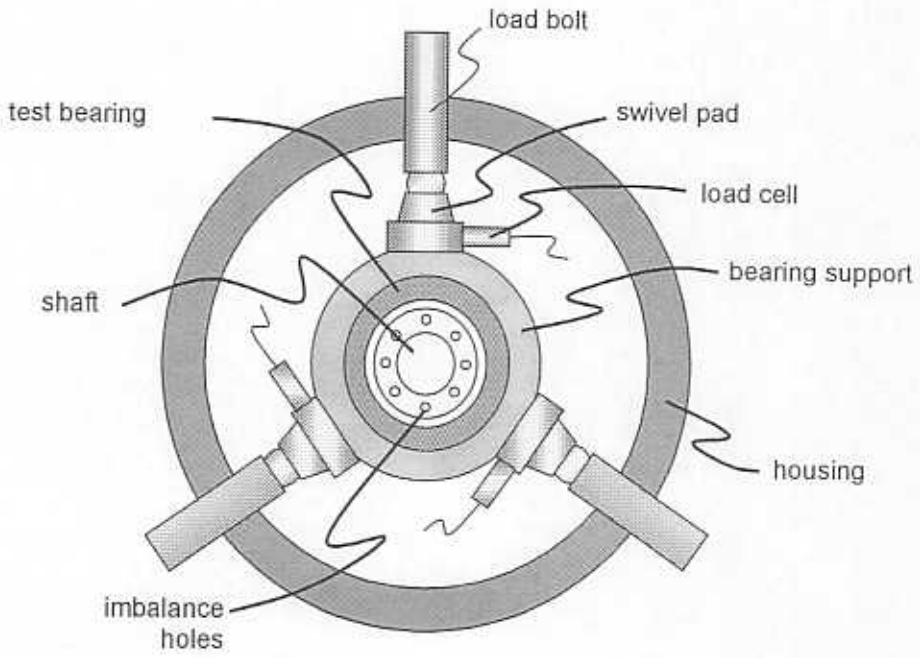

Fig. 5. Axial section at bearings location

Table 1. Load Cells Characteristics[1]

Range	kN [lb]	0.4448 [100]
Resolution	kN [lb]	8.896e-6 [0.002]
Sensitivity	mV/kN [mv/lb]	11241 [50]
Resonant Frequency	kHz	70
Rise Time	μ sec	10
Discharge Time Const.	sec	>500
Low Freq. Resp. (-5%)	Hz	0.001
Amplitude Non-Linearity	% F.S.	1
Stiffness	kN/μm [lb/μin]	17.5 [100]

[1] From PCB Piezotronics, 1998

Thrust pins at both sides of the shaft ensure proper axial positioning of the rotor. The pins consist on a hollow bolt with a ball at the tip and a preloaded spring that keeps the ball in position (See Figure 6). When force is applied to the ball I the axial direction it is set free to rotate in any direction, thus allowing free motion of the rotor in the radial direction. The axial stiffness of the spring is estimated 20 kN/m (Vlier, 1998). Two different sets of pins have been acquired. One with steel balls and one with polymer balls. The polymer balls should provide a self-lubricating surface with better dynamic performance. However, concerns about resistance to wearing of the polymer ball support the acquisition of the steel ball pins as an alternative option.

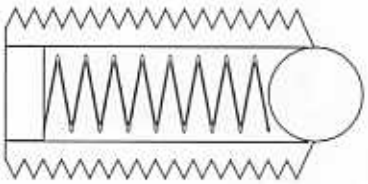

Fig. 6. Thrust pin

High-frequency, high-sensitivity eddy current displacement sensors are installed in the vertical and horizontal direction on both ends of the rotor. The selected sensors, usually employed to measure minute deformations on ball bearing races, are appropriate for the ranges of amplitude and frequency encountered in this application. Table 2 gives relevant information about the nominal sensors' performance. Note that the sensor frequency response is acceptable on the whole range of operation, see Figure 7. The inductance on the tip of the sensor is shielded so that the electromagnetic field is directed towards the front of the sensor, reducing the possibility of "cross-talking" between the vertical and horizontal sensors. This is particularly interesting since, due to geometric restrictions, the two probes need to be installed on the same axial plane. A calibration of the probes on the actual material and geometry is required.

BENTLY NEVADA CORPORATION

SPECIFICATION

Page: 34 of 37	No: 156873	Rev: A 24 Jun 1993
Effective date: 17 May 1993	Prepared by: Tom Calhoun	
Code ID No.: 20230	Approved by:	

Subject: 3300 REBAM transducer: Performance specification

Both Systems

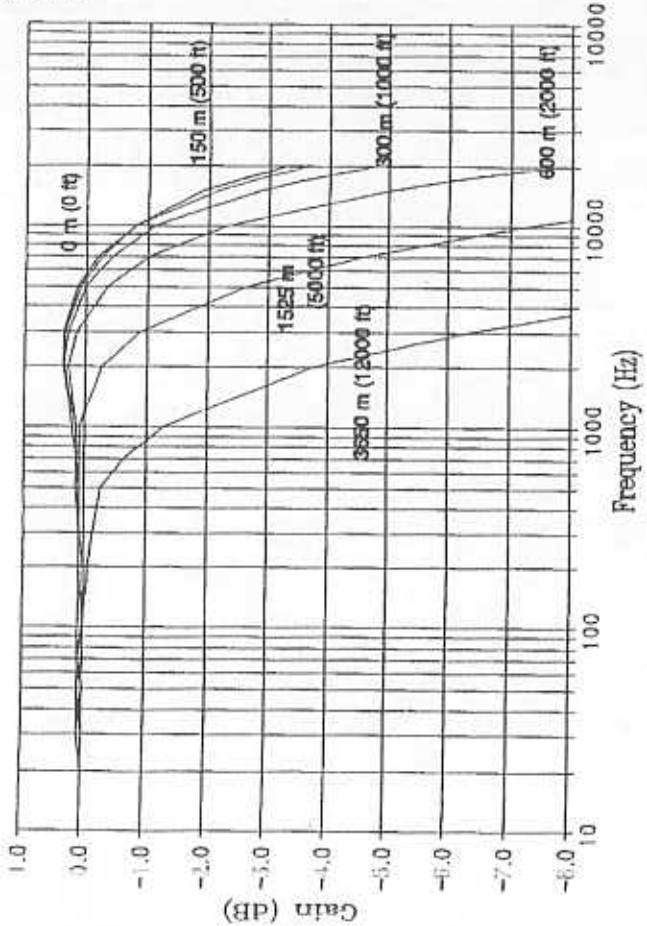

Figure 21. Frequency Response with Output Cable Attached

BENTLY NEVADA CORPORATION

SPECIFICATION

Page: 36 of 37	No: 156873	Rev: A 24 Jun 1993
Effective date: 17 May 1993	Prepared by: Tom Calhoun	
Code ID No.: 20230	Approved by:	

Subject: 3300 REBAM transducer: Performance specification

Both Systems

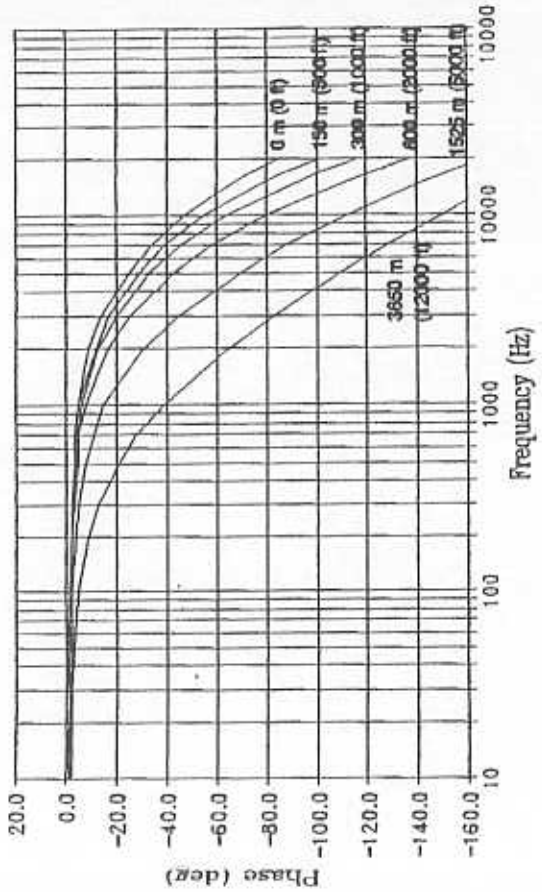

Figure 23. Phase Change vs. Frequency with Output Cable Attached

Fig. 7 Frequency response of displacement transducers

Table 2. Displacement sensors dynamic performance

Supply Voltage	V	24
Supply Current	mA	12
Sensitivity	mV/μm [V/mil]	40 [1]
Linear Range	μm [mil]	400 [16]
Minimum Target Size	mm	9.5
Frequency Response (+5%)	kHz	0 - 10

[2] From Bently Nevada, 1995

3.2 Press-Fit, Stresses and Overall Safety

The high operating speeds of the test rig require extra caution to ensure safe operation of the test rig and to minimize risks in case of an abnormal condition or failure. Based on general rules of thumb given by Sonnichsen (1993), the steel housing is designed with wall thickness of 10 mm or more to avoid penetration of rotor fragments in case of a sudden rotor fracture into small parts. In the case of a complete rotor burst, and assuming that the rotor stops spinning upon contact with the housing, the angular momentum of the rotor (estimated as 0.613 $kg.m^2/s$) is completely transferred to the housing structure. Assuming a conservative time interval of 0.001 sec. for the duration of the impact, the average torque applied to the structure during the impact would be 613 N.m. A wide, solid steel base plate is devised to stand this torque and to provide a firm attachment to ground, preventing the rig to come loose in the event of an impact.

Still, the kinetic energy of the rotor is roughly 2 kJ at maximum speeds. In the case of a burst, most of this energy would be converted into plastic deformation of the casing, heat and noise. The severity of the damages produced to the casing while absorbing this energy is hard to quantify and would depend on the particular failure mechanism of the rotor. A special mechanism is devised in the test rig to direct this energy into a controlled dissipation mechanism. Only the central section of the rig, where the motor is installed, is fixed to ground. The left and right parts of the housing, where the test bearings are installed, fit tightly on a shoulder on the center section. A retainer ring provides a controlled pressure on the contact thus keeping the end sections in place, see Figures 3 and 8. The only force preventing the housing end sections (and the bearings) from rotating is the dry friction between them and the center housing section. Since the smaller clearance between rotating and moving parts is at the bearings, they represent the first point likely to result in contact or impact. In such case, rotation will be induced on the bearing and its support structure thus resulting in relative

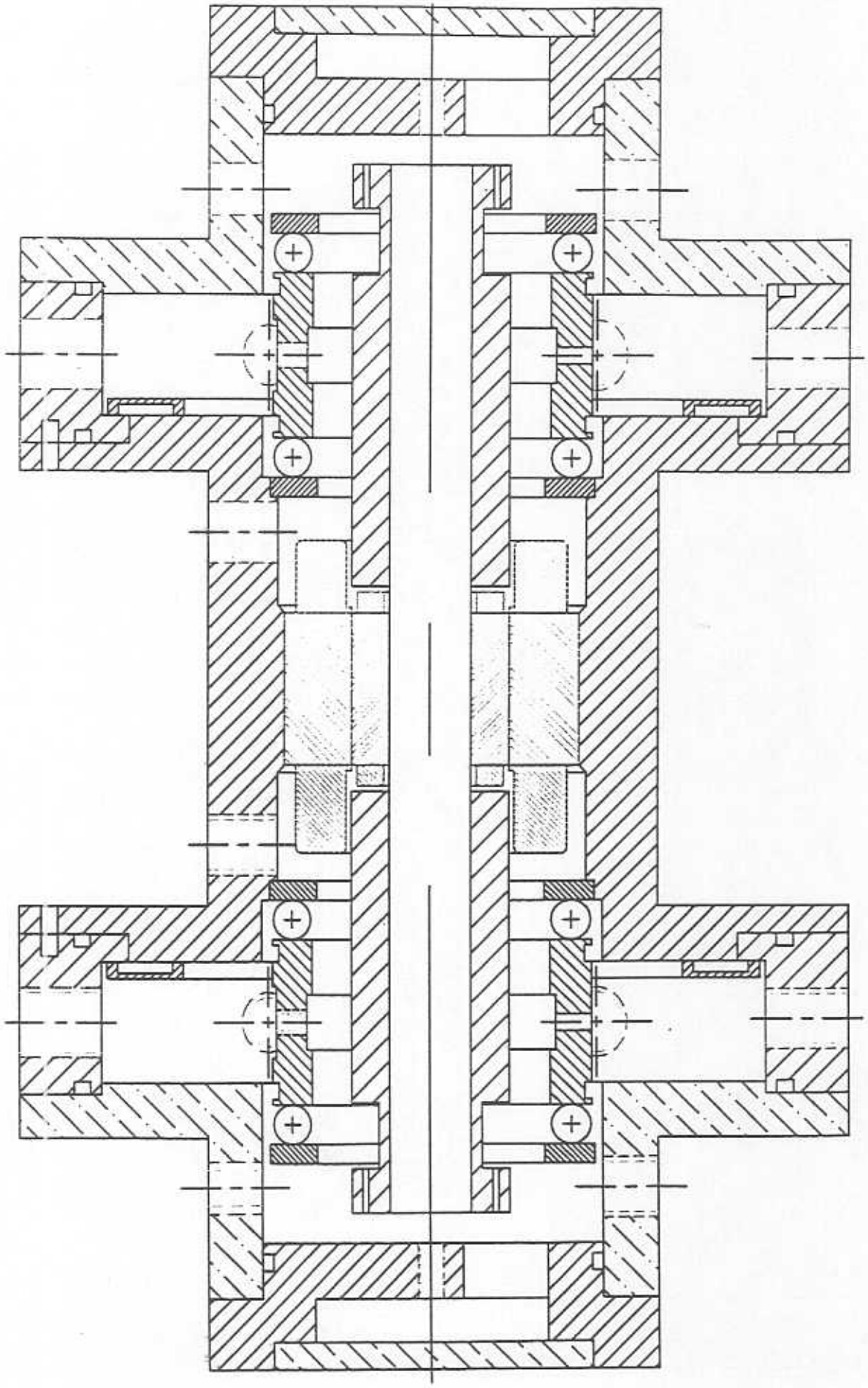

Fig. 8 Test rig assembly, 1:1 scale

motion between the two housing parts. This activates a mechanism that dissipates energy by dry friction in a much longer period of time thus reducing the possibility of a catastrophic failure. A safety enclosure made sandwiched sand between two steel layers provides noise insulation and extra safety in case of sudden burst.

The stresses induced by the high rotational speed affect the size of the rotor parts and the interference on the press fits. The manufacturer of the motor recommends a s6-H6 press fit between the motor element and the shaft and maximum surface speed of 150 m/s for safe operation with a reasonable safety factor (Oberg et al., 1996). This limits the maximum rig speed to 98,835 rpm, which is high enough for our test purposes. The sleeves are designed are designed to use the same press-fit specified for the motor, thus simplifying the manufacturing process. Standard formulas for press-fit and centrifugal strain and stress are used to compute the deformation and stress of both the sleeves and the shaft (Shigley and Mischke, 1996). The specified fit ensures contact between the two rotor parts on the entire range of operating speeds. Table 3 shows the maximum and minimum values possible for the interference. Table 3 also shows the possible range of variation of the journal outer diameter at the location of the bearings, which must be considered for the bearings design. Table 4 shows the maximum effective surface stresses on the shaft and sleeves for the zero and full speed conditions. The maximum predicted stress is 490 MPa, which provides a safety factor of 1.33 (compared to the 655 MPa yield strength for normalized AISI 4140 steel, Avalone and Baumeister, 1996). Appendix A compiles detailed results of the computation of rotor stress an deformation.

Table 3. Resultant radial press fit interference between shaft and sleeves [mm]

	maximum	minimum
at zero speed	0.01950	0.00850
at full speed (100,000 rpm)	0.01412	0.00312
Outer Diameter Growth	0.00226	0.00224

Table 4. Maximum effective surface stress due to press fit and rotation [MPa]

	sleeve		shaft	
	maximum	minimum	maximum	minimum
at zero speed	470.3	205.2	393.1	171.4
at full speed (100,000 rpm)	490.3	229.0	275.0	55.6

3.3 Rotordynamic Performance of the Test Rotor

Figure 9 depicts the rotordynamic model of the rotor shown in Figure 2. The rotor is divided into 38 stations with L/D ratios ranging from 0.15 to 0.40. Typical values of steel density and elasticity/shear modulus are used for the solid shaft and sleeves (ρ=0.27 lb/in, E=29.0e6 psi, G= 11.6e6 psi). Material properties specified by the motor manufacturer are devised for the electric motor rotor (ρ=0.096 lb/in, E=10.2e6 psi, G= 3.8e6 psi). Appendix B contains the numerical data corresponding to the rotor stations as input into the rotordynamic code XL-rotor ™.

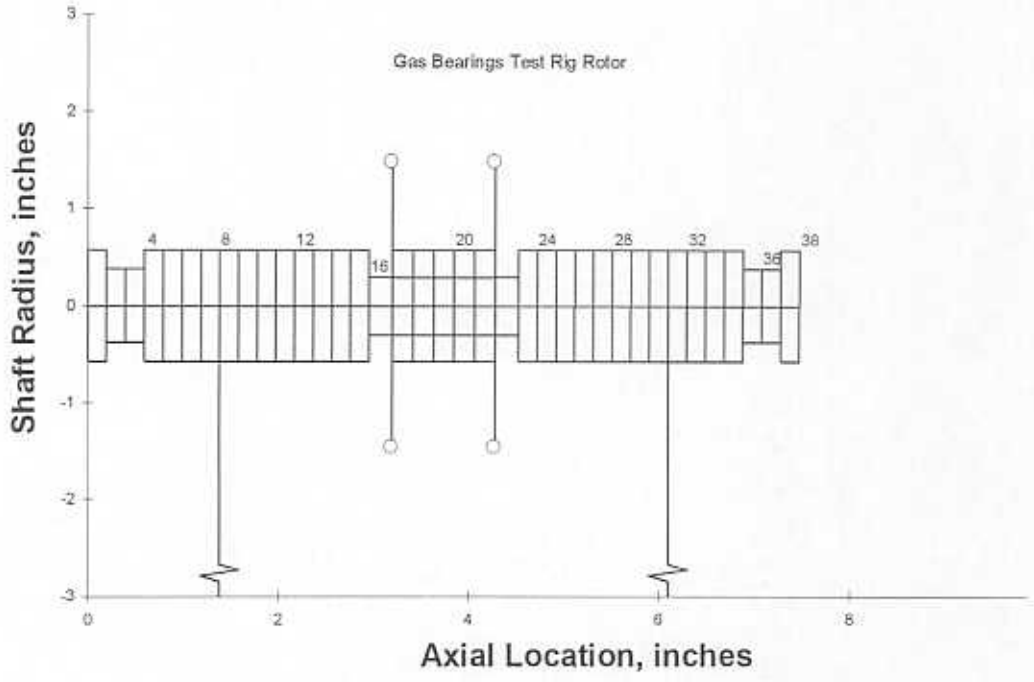

Fig. 9 Rotordynamic rotor model

Figure 10 shows the free-free natural frequencies as a function of the rotational speed. The first bending mode occurs at a frequency of 140,000 cpm and never falls within the range of operating speeds. The second bending mode presents a natural frequency of nearly 420,000

rpm. Figure 11 shows the first bending mode shape. In this mode, most of the shaft deflection occurs in the two sections between the motor and the sleeves while the rest of the shaft remains almost undeformed. Note that the nodal points are just inboard of the bearing locations.

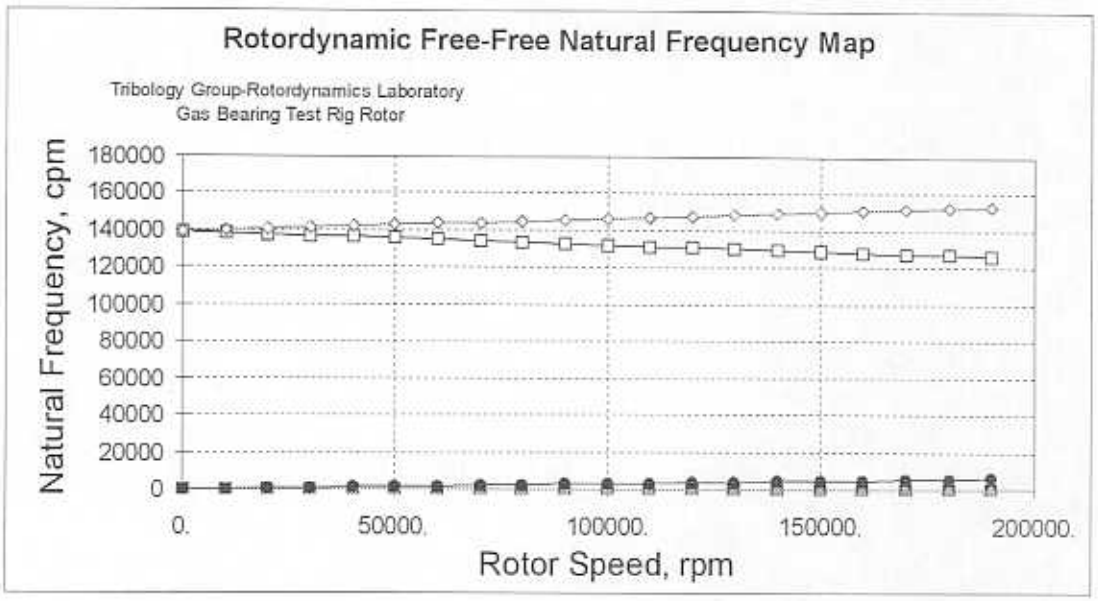

Fig. 10 Free-free natural frequency map

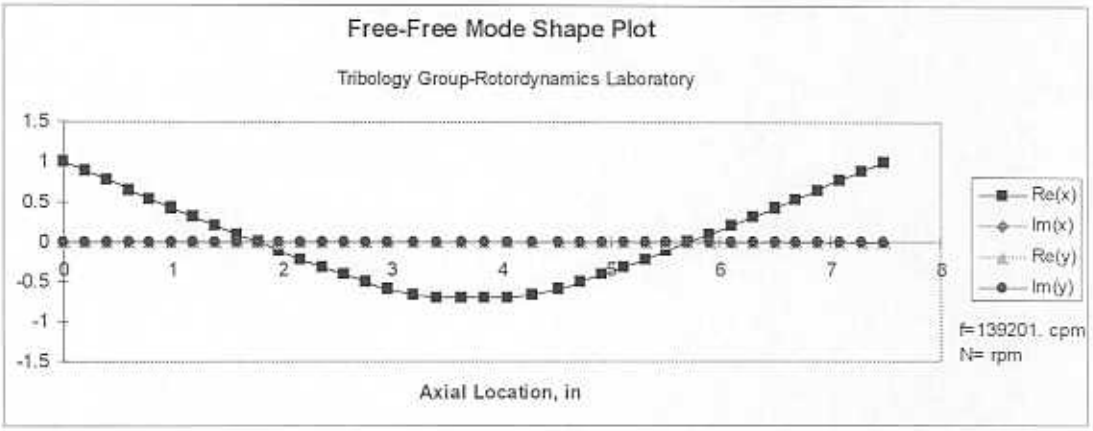

Fig. 11 First bending mode shape

Figure 12 depicts the undamped critical speeds as a function of the bearing stiffness. The critical speeds of the two lower modes are proportional to the bearing stiffness. The critical speeds of the third and fourth modes are practically unaffected by the stiffness of the bearings, perhaps due to the closeness of the bearing locations to the nodal points. Figure 13 shows typical mode shapes corresponding to the first three modes, cylindrical, conical and first bending mode, for a bearing stiffness of 1000 lb/in. The three mode shapes remain almost unaltered for increasing values of bearing stiffness within the range of interest. Note that the first two modes are perfectly rigid body vibration modes, i.e., there no deformation of the shaft on this two modes, the only ones within the operating range.

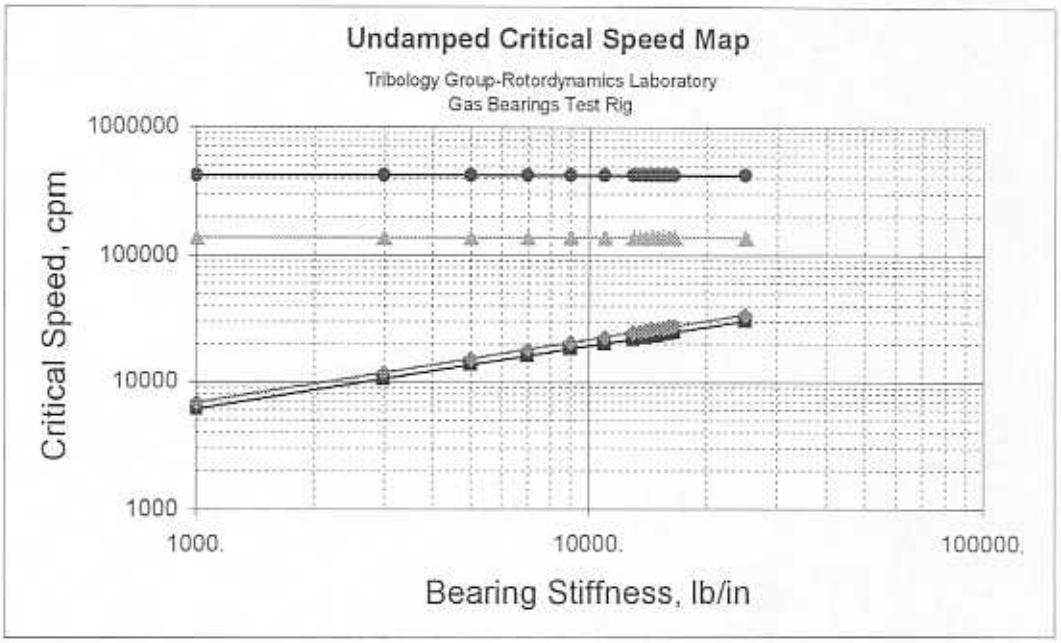

Fig. 12 Undamped critical speed map

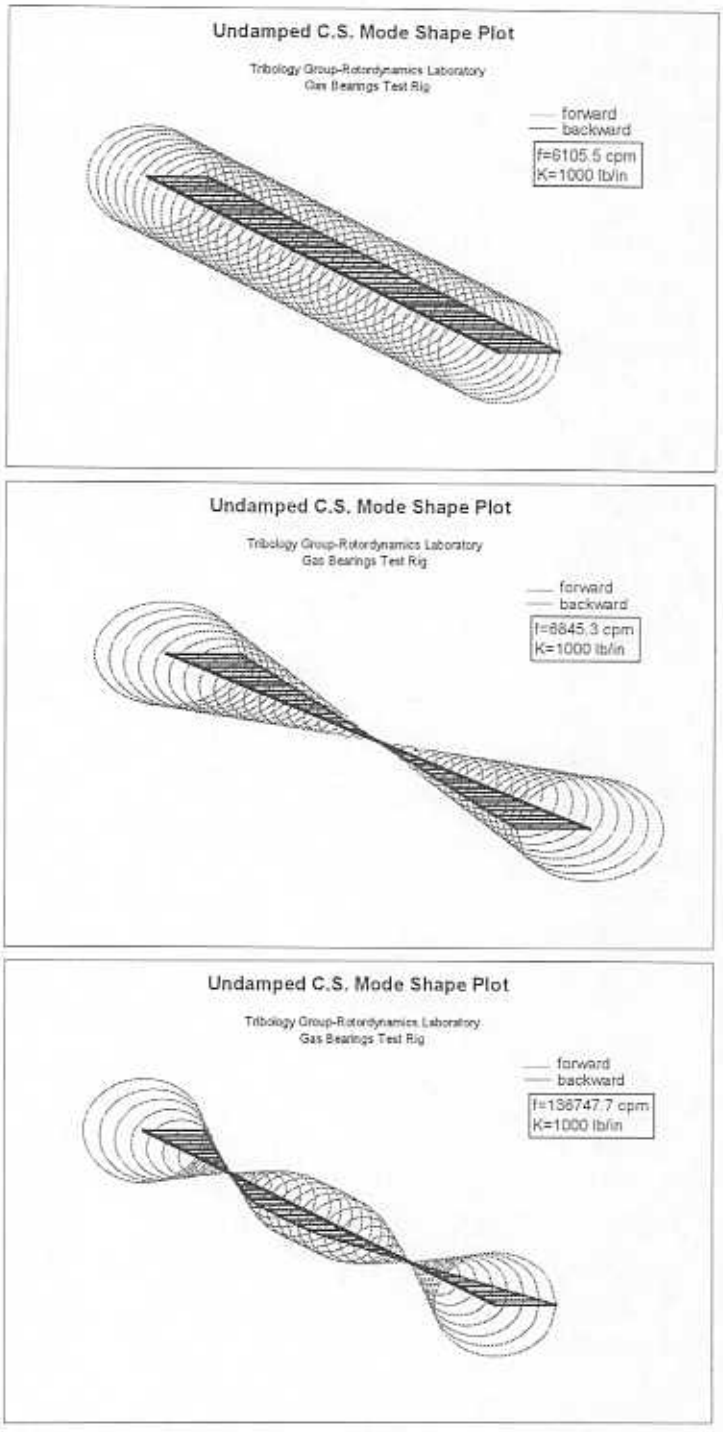

Fig. 13 First three operating mode shapes

Figure 14 shows the predicted response amplitude at the shaft end for coupled unitary (1 gram-in) imbalances placed 180° out of phase at each end of the shaft. Since no other mode is excited, the response shows a single critical speed as it is typical on one degree of freedom systems. Above the critical speed the vibration tends to stabilize at a value presumably corresponding to the self-balancing condition. For this case, with a bearing stiffness of 1,000 lb/in, the critical speed corresponds to about 10,000 rpm. Figure 15 shows the force transmitted to the bearing to follow a trend similar to that of the motion amplitude, starting from zero, reaching a maximum at the critical speed and then approaching a stable value.

Figure 16 shows the deflected mode shape at 10,000 rpm and 100,000 rpm. On the whole range of operating speeds the shaft remains (nearly) rigid when excited by imbalance weights 180° out of phase, i.e., when only the conical mode is excited.

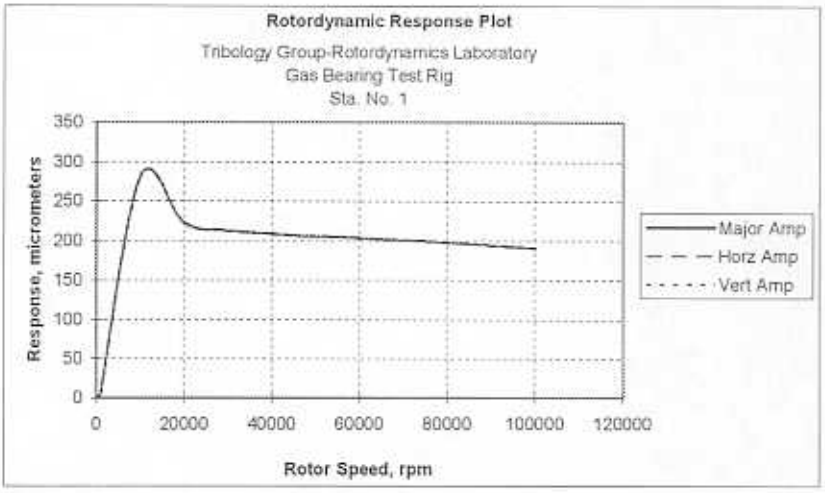

Fig. 14 Amplitude of vibration for unit (1 gm-in) imbalances 180° out of phase (K_{brg}=1000 lb/in)

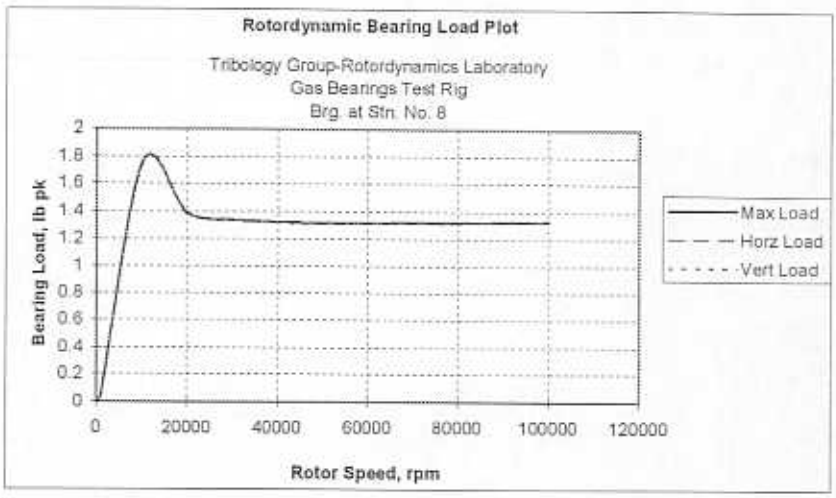

Fig. 15 Force transmitted through the bearing for unit (1 gm-in) imbalances 180° out of phase (K_{brg}=1000 lb/in)

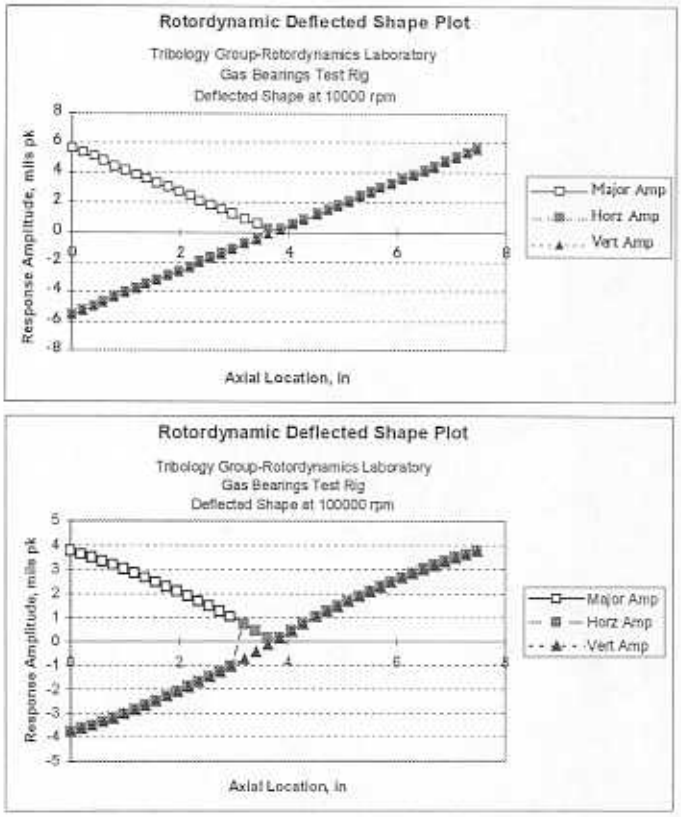

Fig. 16 Deflectected shapes for unit (1 gm-in) imbalances 180° out of phase at 10,000 and 100,000 rpm (K_{brg}=1000 lb/in)

Figure 17 shows the predicted response amplitude at the shaft end for coupled unitary (1 gram-in) imbalances placed in phase at each end of the shaft. Figure 18 depicts the corresponding force transmitted to the bearings. Figure 19 compiles the deflected shapes at 10, 40 and 100 krpm. At low speeds only the cylindrical mode has significant contributions to the dynamic response. However, from mid to high speeds the contribution of the first bending mode is important. Above 60,000 rpm the amplitude of motion starts to increase under the effect of the first bending mode. At the same time the transmitted force decreases reaching an almost null value at full speed. Figure 19 shows how the deflected shape (combination of the cylindrical and the first bending mode) presents nodes almost coinciding with the location of the bearings at 100,000 rpm, which explains why the transmitted force is so small at this speed.

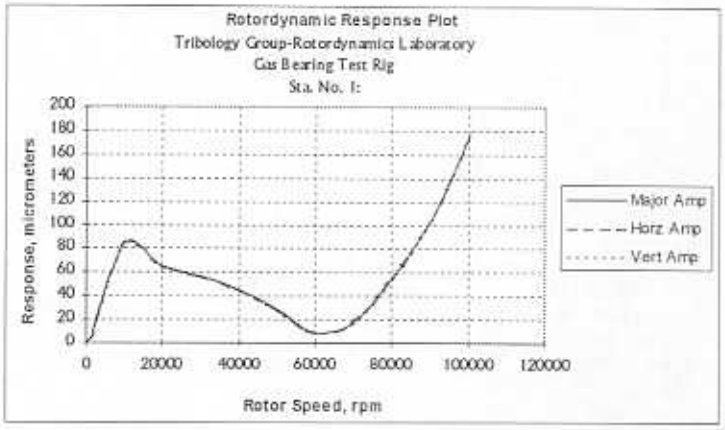

Fig. 17 Amplitude of vibration for unit (1 gm-in) imbalances in phase (K_{brg}=1000 lb/in)

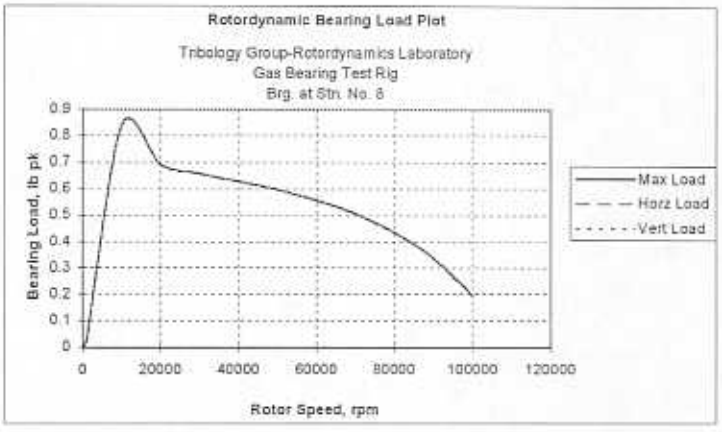

Fig. 18 Force transmitted through the bearing for unit (1 gm-in) imbalances in phase (K_{brg}=1000 lb/in)

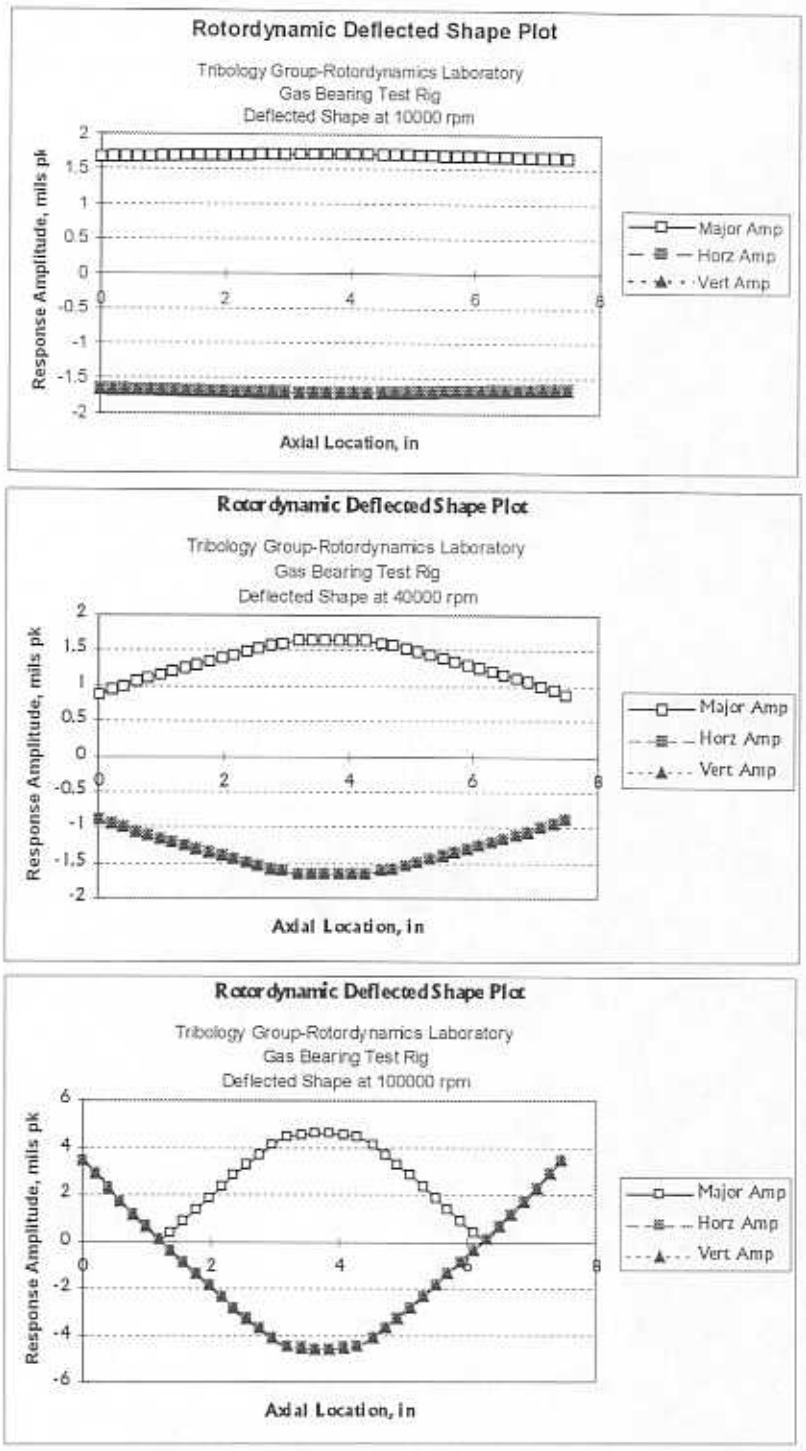

Fig. 19 Defelctected shapes for unit (1 gm-in) imbalances in phase at 10,000 and 100,000 rpm (K_{brg}=1000 lb/in)

9. CONCLUSIONS AND RECOMMENDATIONS

The detailed design of a new test rig for the analysis of the dynamic performance of gas bearings is presented. Details on the selection of the instrumentation, including appropriate displacement and force sensors, as well as a suitable tachometer, are summarized. Special attention has been paid to safety issues since the experimental prototype is to run at extremely high speeds.

A full set of detailed drawings (23 in total) for the manufacturing of the test rig has been prepared. Currently, the test rig is in the process of manufacturing. The instrumentation and electric motor and drive have already been purchased. The test rig is expected to be fully operative and debugged for the fall 99 semester, when the experimental phase is scheduled to start.

The new test facility allows analysis of the forced vibration of a rigid rotor supported on gas bearings operating at high speeds. Several designs of bearings can be easily installed on the rig, including hydrodynamic, hydrostatic or hybrid bearings. The rig is fully instrumented to measure rotor vibration and forces transmitted to the supports. Run-up and coast-down tests with increasing levels of disk imbalances will be performed to measure the rotordynamic forced response and to extract equivalent stiffness and damping coefficients of the air bearings. Experiments are also aimed at determining the lift-off speed and "break" torque at which the rotor runs freely on a hydrodynamic air cushion created by the air bearings.

The research offers an opportunity to test the viability of air bearing technology for oil-free, high speed rotating machinery and to advance the state-of-the-art analysis of micro film thickness air bearings and seals. The applicability of the analysis and test results covers a wide range, from large scale aircraft engine propulsion systems and secondary power units for space cryogenic turbopumps to automotive turbochargers, *APU*'s, compact compressors for air conditioning, space life support systems and fast data computer storage units.

REFERENCES

Avallone, E.A., and Baumeister, T., 1996, *Mark's Standard Handbook for Mechanical Engineering*, tenth edition, McGraw Hill, New York.

Bently Nevada Corp., 1995, *Transducers*, Minden, Nevada.

Kline, S. J., and McClintock, F.A., 1953, "Describing Uncertainties in Single-Sample Experiments," *ASME* Mechanical Engineering, Vol. 75, pp. 3-8.

Oberg, E., Jones, F., Horton, H., and Riffel, H., 1996, *Machinery's Handbook*, Industrial Press Inc. New York.

PCB Piezotronics, 1998, *ICP® Force Sensor, General Operation Manual*, Depew, New York.

Shigley, J.E., and Mischke, C.R., 1996, *Standard Hanbook of Machine Design*, second edition, McGraw-Hill, N.Y.

Sonnischsen, H., 1993, "Ensuring Spin Test Safety," Mechanical Engineering, Vol. 115, No. 12, ASME, pp. 72-77.

Vlier Engineering, 1988, *Pocket Catalog*, New York.

APPENDIX A

PRESS FIT AND CENTRIFUGAL ROTOR STRESS AND DEFORMATION
(Input and output pages of the code FIT, version 2.21,
by Rotordynamics-Seal Research, 1995)

FIT VERSION 2.21, RELEASE DATE 2/1/95
SUMMARY OF INPUT

1	units (0 = ENGLISH, 1 = SI)
25.00	ambient temperature (C)
25.00	operating temperature shaft (C)
25.00	operating temperature sleeve (C)
-17.78	operating temperature insert (C)
25.00	operating temperature housing (C)
25.00	storage temp. of the machine (C)
100000.00	operating shaft speed (rpm)
1	shaft sleeve (0 = NO, 1 = YES)
0	housing insert (0 = NO, 1 = YES)
15.03500	O.D. shaft maximum at amb temp (mm)
15.03000	O.D. shaft minimum at amb temp (mm)
15.00000	effective shaft O.D. at amb temp (mm)
0.00000	effective shaft I.D. at amb temp (mm)
29.00000	O.D. sleeve maximum at amb temp (mm)
29.00000	O.D. sleeve minimum at amb temp (mm)
15.01000	I.D. sleeve maximum at amb temp (mm)
15.00000	I.D. sleeve minimum at amb temp (mm)
29.00000	effective sleeve O.D. at amb temp (mm)
15.00000	effective sleeve I.D. at amb temp (mm)
0.00000	O.D. insert maximum at amb temp (mm)
0.00000	O.D. insert minimum at amb temp (mm)
0.00000	I.D. insert maximum at amb temp (mm)
0.00000	I.D. insert minimum at amb temp (mm)
30.00000	I.D. housing max at ambient temp (mm)
30.00000	I.D. housing min at ambient temp (mm)
50.00000	effective housing O.D. (mm)
User Defined	shaft material name
7.84880	density of shaft (g/cm^3)
0.1130E-04	thermal expansion coef. for shaft (1/C)
0.2070E+06	youngs modulus for shaft (MPa)
0.29000	poissons ratio for shaft (-)
User Defined	sleeve material name
7.84880	density of sleeve (g/cm^3)
0.1130E-04	thermal expansion coef. for sleeve (1/C)
0.2070E+06	youngs modulus for sleeve (MPa)
0.29000	poissons ratio for sleeve (-)
User Defined	insert material name
0.0000E+00	thermal expansion coef. for insert (1/C)
0.0000E+00	youngs modulus for insert (MPa)
0.00000	poissons ratio for insert (-)
User Defined	housing material name
0.1130E-04	thermal expansion coef. for housing (1/C)
0.2070E+06	youngs modulus for housing (MPa)
0.29000	poissons ratio for housing (-)

SUMMARY OF RESULTS

RESULTANT RADIAL CLEARANCE BETWEEN ROTOR/STATOR (mm)
NEGATIVE VALUES INDICATE INTERFERENCE FIT

max	min	
0.50000	0.50000	at ambient, temp freestanding
0.49483	0.49097	at ambient temp, assembled
0.49258	0.48871	at operating conditions
0.49483	0.49097	at storage temp

RESULTANT RADIAL PRESS FIT BETWEEN SHAFT/SLEEVE (mm)
NEGATIVE VALUES INDICATE CLEARANCE FIT

max	min	
0.01750	0.01000	at ambient temp, freestanding
0.01750	0.01000	at ambient temp, assembled
0.01212	0.00462	at operating conditions
0.01750	0.01000	at storage temp

SHAFT STRESS COMPONENTS DUE TO PRESS FIT
AT MAXIMUM EFFECTIVE STRESS LOCATION (MPa)
NEGATIVE VALUES INDICATE COMPRESSIVE STRESS

TANGENTIAL		RADIAL		
max	min	max	min	
0.0000E+00	0.0000E+00	0.0000E+00	0.0000E+00	at ambient temp, freestanding
-0.3529E+03	-0.2016E+03	0.0000E+00	0.0000E+00	at ambient temp, assembled
-0.2443E+03	-0.9305E+02	0.0000E+00	0.0000E+00	at operating conditions
-0.3529E+03	-0.2016E+03	0.0000E+00	0.0000E+00	at storage temp

SLEEVE STRESS COMPONENTS DUE TO PRESS FIT
AT MAXIMUM EFFECTIVE SURFACE STRESS LOCATION (MPa)
NEGATIVE VALUES INDICATE COMPRESSIVE STRESS

TANGENTIAL		RADIAL		
max	min	max	min	
0.0000E+00	0.0000E+00	0.0000E+00	0.0000E+00	at ambient temp, freestanding
0.3053E+03	0.1746E+03	-0.1764E+03	-0.1008E+03	at ambient temp, assembled
0.2114E+03	0.8061E+02	-0.1221E+03	-0.4652E+02	at operating conditions
0.3053E+03	0.1746E+03	-0.1764E+03	-0.1008E+03	at storage temp

STRESS DUE TO ROTATION
AT MAXIMUM EFFECTIVE SURFACE STRESS LOCATION (MPa)

TANGENTIAL	RADIAL	
0.1997E+02	0.1997E+02	Shaft Stress
0.1572E+03	0.0000E+00	Sleeve Stress

MAXIMUM EFFECTIVE SURFACE STRESS DUE TO PRESS FIT AND ROTATION (MPa)

SLEEVE		SHAFT		
max	min	max	min	
0.0000E+00	0.0000E+00	0.0000E+00	0.0000E+00	at ambient temp, freestanding
0.4222E+03	0.2413E+03	0.3529E+03	0.2016E+03	at ambient temp, assembled
0.4425E+03	0.2642E+03	0.2349E+03	0.8485E+02	at operating conditions
0.4222E+03	0.2413E+03	0.3529E+03	0.2016E+03	at storage temp

APPENDIX B

ROTORDYNAMIC ROTOR MODEL
(input pages to the code XL-rotor ™)

INPUT TABLE OF BEAM AND STATION DEFINITIONS, MORE THAN ONE BEAM PER STATION IS OK									
Station	Length	OD	ID	Weight Density	Elastic Modulus	Shear Modulus	Added Weight	Added Ip	Added It
#	in	in	in	lb/in^3	psi	psi	lb	lb-in^2	lb-in^2
1	0.19685	1.1417	0	0.27	29.0E+6	11.6E+6	0.0	0.0	0.0
2	0.19685	0.748	0	0.27	29.0E+6	11.6E+6	0.0	0.0	0.0
3	0.19685	0.748	0	0.27	29.0E+6	11.6E+6	0.0	0.0	0.0
4	0.19685	0.748	0	0.27	29.0E+6	11.6E+6	0.0	0.0	0.0
5	0.19685	1.1417	0	0.27	29.0E+6	11.6E+6	0.0	0.0	0.0
6	0.19685	1.1417	0	0.27	29.0E+6	11.6E+6	0.0	0.0	0.0
7	0.19685	1.1417	0	0.27	29.0E+6	11.6E+6	0.0	0.0	0.0
8	0.19685	1.1417	0	0.27	29.0E+6	11.6E+6	0.0	0.0	0.0
9	0.19685	1.1417	0	0.27	29.0E+6	11.6E+6	0.0	0.0	0.0
10	0.19685	1.1417	0	0.27	29.0E+6	11.6E+6	0.0	0.0	0.0
11	0.19685	1.1417	0	0.27	29.0E+6	11.6E+6	0.0	0.0	0.0
12	0.19685	1.1417	0	0.27	29.0E+6	11.6E+6	0.0	0.0	0.0
13	0.19685	1.1417	0	0.27	29.0E+6	11.6E+6	0.0	0.0	0.0
14	0.19685	1.1417	0	0.27	29.0E+6	11.6E+6	0.0	0.0	0.0
15	0.19685	1.1417	0	0.27	29.0E+6	11.6E+6	0.0	0.0	0.0
16	0.2441	0.5906	0	0.27	29.0E+6	11.6E+6	0.0	0.0	0.0
17	0.21732	0.5906	0	0.27	29.0E+6	11.6E+6	0.007693	0.001517	0.000773
17	0.21732	1.1417	0.5906	0.096	10.2E+6	3.8E+6	0.0	0.0	0.0
18	0.21732	0.5906	0	0.27	29.0E+6	11.6E+6	0.0	0.0	0.0
18	0.21732	1.1417	0.5906	0.096	10.2E+6	3.8E+6	0.0	0.0	0.0
19	0.21732	0.5906	0.	0.27	29.0E+6	11.6E+6	0.0	0.0	0.0
19	0.21732	1.1417	0.5906	0.096	10.2E+6	3.8E+6	0.0	0.0	0.0
20	0.21732	0.5906	0	0.27	29.0E+6	11.6E+6	0.0	0.0	0.0
20	0.21732	1.1417	0.5906	0.096	10.2E+6	3.8E+6	0.0	0.0	0.0
21	0.21732	0.5906	0	0.27	29.0E+6	11.6E+6	0.0	0.0	0.0
21	0.21732	1.1417	0.5906	0.096	10.2E+6	3.8E+6	0.0	0.0	0.0
22	0.2441	0.5906	0.	0.27	29.0E+6	11.6E+6	0.007693	0.001517	0.000773
23	0.19685	1.1417	0.	0.27	29.0E+6	11.6E+6	0.0	0.0	0.0
24	0.19685	1.1417	0.	0.27	29.0E+6	11.6E+6	0.0	0.0	0.0
25	0.19685	1.1417	0	0.27	29.0E+6	11.6E+6	0.0	0.0	0.0
26	0.19685	1.1417	0	0.27	29.0E+6	11.6E+6	0.0	0.0	0.0
27	0.19685	1.1417	0	0.27	29.0E+6	11.6E+6	0.0	0.0	0.0
28	0.19685	1.1417	0	0.27	29.0E+6	11.6E+6	0.0	0.0	0.0
29	0.19685	1.1417	0	0.27	29.0E+6	11.6E+6	0.0	0.0	0.0
30	0.19685	1.1417	0	0.27	29.0E+6	11.6E+6	0.0	0.0	0.0
31	0.19685	1.1417	0	0.27	29.0E+6	11.6E+6	0.0	0.0	0.0
32	0.19685	1.1417	0	0.27	29.0E+6	11.6E+6	0.0	0.0	0.0
33	0.19685	1.1417	0.	0.27	29.0E+6	11.6E+6	0.0	0.0	0.0
34	0.19685	0.748	0	0.27	29.0E+6	11.6E+6	0.0	0.0	0.0
35	0.19685	0.748	0	0.27	29.0E+6	11.6E+6	0.0	0.0	0.0
36	0.19685	0.748	0	0.27	29.0E+6	11.6E+6	0.0	0.0	0.0
37	0.19685	1.1417	0	0.27	29.0E+6	11.6E+6	0.0	0.0	0.0
38	0	1.1417	0	0.27	29.0E+6	11.6E+6	0.0	0.0	0.0

SUMMARY TABLE OF ALL BEAMS DEFINED IN MODEL							
Beam Number	Station #	Axial Location	Beam Weight	Beam It	Beam Ip	Beam EI	Beam GA
		in	lb	lb-in^2	lb-in^2	lb-in^2	lb
1	1	0	0.054412	0.004608	0.008866	2.4E+6	11.9E+6
2	2	0.19685	0.023356	0.000892	0.001633	445.6E+3	5.1E+6
3	3	0.3937	0.023356	0.000892	0.001633	445.6E+3	5.1E+6
4	4	0.59055	0.023356	0.000892	0.001633	445.6E+3	5.1E+6
5	5	0.7874	0.054412	0.004608	0.008866	2.4E+6	11.9E+6
6	6	0.98425	0.054412	0.004608	0.008866	2.4E+6	11.9E+6
7	7	1.1811	0.054412	0.004608	0.008866	2.4E+6	11.9E+6
8	8	1.37795	0.054412	0.004608	0.008866	2.4E+6	11.9E+6
9	9	1.5748	0.054412	0.004608	0.008866	2.4E+6	11.9E+6
10	10	1.77165	0.054412	0.004608	0.008866	2.4E+6	11.9E+6
11	11	1.9685	0.054412	0.004608	0.008866	2.4E+6	11.9E+6
12	12	2.16535	0.054412	0.004608	0.008866	2.4E+6	11.9E+6
13	13	2.3622	0.054412	0.004608	0.008866	2.4E+6	11.9E+6
14	14	2.55905	0.054412	0.004608	0.008866	2.4E+6	11.9E+6
15	15	2.7559	0.054412	0.004608	0.008866	2.4E+6	11.9E+6
16	16	2.95275	0.018055	0.000483	0.000787	173.2E+3	3.2E+6
17	17	3.19685	0.016075	0.000414	0.000701	173.2E+3	3.2E+6
18	17	3.19685	0.015643	0.001677	0.003231	785.9E+3	2.8E+6
19	18	3.41417	0.016075	0.000414	0.000701	173.2E+3	3.2E+6
20	18	3.41417	0.015643	0.001677	0.003231	785.9E+3	2.8E+6
21	19	3.63149	0.016075	0.000414	0.000701	173.2E+3	3.2E+6
22	19	3.63149	0.015643	0.001677	0.003231	785.9E+3	2.8E+6
23	20	3.84881	0.016075	0.000414	0.000701	173.2E+3	3.2E+6
24	20	3.84881	0.015643	0.001677	0.003231	785.9E+3	2.8E+6
25	21	4.06613	0.016075	0.000414	0.000701	173.2E+3	3.2E+6
26	21	4.06613	0.015643	0.001677	0.003231	785.9E+3	2.8E+6
27	22	4.28345	0.018055	0.000483	0.000787	173.2E+3	3.2E+6
28	23	4.52755	0.054412	0.004608	0.008866	2.4E+6	11.9E+6
29	24	4.7244	0.054412	0.004608	0.008866	2.4E+6	11.9E+6
30	25	4.92125	0.054412	0.004608	0.008866	2.4E+6	11.9E+6
31	26	5.1181	0.054412	0.004608	0.008866	2.4E+6	11.9E+6
32	27	5.31495	0.054412	0.004608	0.008866	2.4E+6	11.9E+6
33	28	5.5118	0.054412	0.004608	0.008866	2.4E+6	11.9E+6
34	29	5.70865	0.054412	0.004608	0.008866	2.4E+6	11.9E+6
35	30	5.9055	0.054412	0.004608	0.008866	2.4E+6	11.9E+6
36	31	6.10235	0.054412	0.004608	0.008866	2.4E+6	11.9E+6
37	32	6.2992	0.054412	0.004608	0.008866	2.4E+6	11.9E+6
38	33	6.49605	0.054412	0.004608	0.008866	2.4E+6	11.9E+6
39	34	6.6929	0.023356	0.000892	0.001633	445.6E+3	5.1E+6
40	35	6.88975	0.023356	0.000892	0.001633	445.6E+3	5.1E+6
41	36	7.0866	0.023356	0.000892	0.001633	445.6E+3	5.1E+6
42	37	7.28345	0.054412	0.004608	0.008866	2.4E+6	11.9E+6
43	38	7.4803	0	0	0	2.4E+6	11.9E+6
			1.64	**0.13**	**0.24**		